International Journal of Plasticity 53 (2014) 179–192

Contents lists available at ScienceDirect

International Journal of Plasticity

journal homepage: www.elsevier.com/locate/ijplas

Disclination mediated plasticity in shear-coupled boundary migration

V. Taupin [a,*], L. Capolungo [b], C. Fressengeas [a]

[a] Laboratoire d'Etude des Microstructures et de Mécanique des Matériaux, Université de Lorraine/CNRS, Ile du Saulcy, 57045 Metz Cedex, France
[b] G.W. Woodruff School of Mechanical Engineering, Georgia Institute of Technology/CNRS, 57070 Metz Cedex, France

ARTICLE INFO

Article history:
Received 12 April 2013
Received in final revised form 24 July 2013
Available online 15 August 2013

Keywords:
Boundary migration
Disclinations
Dislocations

ABSTRACT

The shear-coupled boundary migration of ⟨001⟩ symmetric tilt boundaries is investigated within the framework of an elasto-plastic theory of disclination and dislocation fields. The tilt boundaries are built from periodic partial wedge-disclination dipole arrays, on the basis of their atomistic topography. Non-locality of the elastic response of the adjacent crystals stems from the defected structure of their boundary. Upon applying a shear strain to the bicrystal, couple stresses are generated, which set the disclination dipole array into motion normal to the boundary. In the process, edge dislocation densities with partial Burgers vector lying along the boundary are nucleated, whose glide parallel to the boundary and annihilation produces plastic shear. The misorientation dependence of the shear coupling factor predicted by the model is in full agreement with data from atomistic simulations and experiments. It is found to depend on the polarity and the magnitude of the wedge disclination dipoles composing the grain boundary.

1. Introduction

Plasticity in polycrystalline media is mediated by a vast diversity of defect nucleation and motion mechanisms (e.g. dislocation glide, vacancy diffusion, dislocation climb, grain boundary migration, grain boundary sliding, etc.). At fixed chemistry, the relative contribution of each mechanism depends on temperature, strain rate, grain size, texture, etc. For example, when the grain size is in the range of tens of nanometers, the role of grain boundaries and triple junctions in so-called nanocrystalline materials become predominant (Gurtin and Anand, 2008). Triple junction and grain boundary migrations are readily activated at moderate temperatures (Mompiou et al., 2009). To deconvolute the role of triple junction motion from that of grain boundary migration, several experimental and theoretical studies have focused on bicrystals (Winning et al., 2001; Cahn et al., 2006; Gorkaya et al., 2009; Berbenni et al., 2013). When a shear stress is applied to a bicrystal, the grain boundary can migrate normal to its axis of symmetry and relax stresses by producing plastic shear. In this process, one crystal grows at the expense of the other by the normal motion (migration) of the grain boundary, and shear/rotation of the material traversed by the grain boundary occurs. Shearing of this region results in the relative motion of the two crystals, parallel to the grain boundary. This essentially non-diffusive mechanism was observed experimentally and modeled for ⟨001⟩ symmetric tilt boundaries in Cu bicrystals by using molecular dynamics methods (Cahn et al., 2006). The coupling of the displacements parallel and normal to the boundary is quantified by a geometrical factor β defined from pure interfacial kinematics considerations (Berbenni et al., 2013). If $u_{\perp}$ and $u_{//}$ denote the distance of normal migration of the grain boundary and the relative displacement of the two crystals produced by shear, respectively, the shear coupling factor is measured by the ratio $\beta = u_{//}/u_{\perp}$. Interestingly, β increases in absolute value with misorientations relative to 0° and 90°, and follows two

* Corresponding author. Address: LEM3, UMR CNRS 7239, University of Lorraine, Ile du Saulcy, 57045 Metz, France.
E-mail address: vincent.taupin@univ-lorraine.fr (V. Taupin).

0749-6419/$ - see front matter © 2013 Elsevier Ltd. All rights reserved.
http://dx.doi.org/10.1016/j.ijplas.2013.08.002

branches of opposite sign, with a sharp switch around 37° (Cahn et al., 2006). This misorientation dependence was retrieved experimentally for ⟨001⟩ symmetric tilt boundaries in Al bicrystals (Gorkaya et al., 2009). Using surface-dislocation-based models of grain boundaries (Frank, 1950; Bilby, 1955), the coupling factor β may be simply obtained from the Burgers vector's content of the interface as a function of the misorientation (Cahn et al., 2006). However, this approach fails to account for the structure and energy of high-angle grain boundaries, because it overlooks their core properties.

In the present paper, we intend to analyze shear coupled boundary migration within the framework of a recently developed elasto-plastic theory of dislocation and disclination fields (Fressengeas et al., 2011). In this approach, the internal stress and couple-stress fields arising from the presence of crystal defects (dislocations and disclinations) are accounted for. Further, nonlocal elastic response in the presence of dislocations and disclinations is assumed, consistent with previous findings (Upadhyay et al., 2013). A field description of the crystal displacements and of its defects through their densities at interatomic resolution length scale then allows describing the structure and core energy of grain boundaries, in excellent agreement with atomistic simulations and experiments (Taupin et al., 2013; Fressengeas et al., 2013). Plasticity derives from the transport of dislocation and disclination densities through the material. Interestingly, the transport equations provide an undisputable kinematic structure for the spatio-temporal evolution of the crystal defect densities. Thermodynamical guidelines allow substantiating this structure with appropriate constitutive relationships for plasticity in terms of driving forces vs. dislocation/disclination velocities (Fressengeas et al., 2011). The theory is used to model the symmetric ⟨001⟩ tilt boundaries in Cu bicrystals previously considered (Fressengeas et al., 2013). Our main objective is to analyze the boundary migration mechanisms in terms of the coupled disclination and dislocation dynamics, and to provide tools for further studies of grain boundary-mediated plasticity. However, other potential mechanisms, such as grain boundary sliding or dislocation emission/absorption, will not be treated in the present paper. The predictions of our theory will be compared with experimental data and other existing approaches, mainly atomistic simulations (Cahn et al., 2006; Farkas et al., 2006; Tucker et al., 2010) and surface-dislocation-based models (Cahn et al., 2006; Berbenni et al., 2013).

The paper is organized as follows. In Section 2, the elasto-plastic theory of disclination and dislocation fields is briefly recalled. More details can be found in reference (Fressengeas et al., 2011) and in the pioneering work of deWit (deWit, 1970). In Section 3, the construction of tilt boundaries with wedge disclination dipoles introduced (Fressengeas et al., 2013), is recalled for completeness. Then, nonlocal elastic constitutive laws are derived, and our results on shear-coupled boundary migration are presented and discussed by comparison with experiments and other modeling approaches. Conclusions follow in Section 4.

2. Elasto-plastic theory of disclination and dislocation fields

2.1. Notations

A bold symbol denotes a tensor. When there may be ambiguity, an arrow is superposed to represent a vector: $\vec{\mathbf{V}}$. The symmetric part of tensor $\mathbf{A}$ is denoted $\mathbf{A}^{sym}$. Its skew-symmetric and deviatoric parts are $\mathbf{A}^{skew}$ and $\mathbf{A}^{dev}$ respectively. The tensor $\mathbf{A}\cdot\mathbf{B}$, with rectangular Cartesian components $A_{ik}B_{kj}$, results from the dot product of tensors $\mathbf{A}$ and $\mathbf{B}$, and $\mathbf{A}\otimes\mathbf{B}$ is their tensorial product, with components $A_{ij}B_{kl}$. The vector $\mathbf{A}\cdot\mathbf{V}$, with rectangular Cartesian components $A_{ij}V_j$, results from the dot product of tensor $\mathbf{A}$ and vector $\mathbf{V}$. A : represents the trace inner product of the two second order tensors $\mathbf{A}:\mathbf{B}=A_{ij}B_{ij}$, in rectangular Cartesian components, or the product of a higher order tensor with a second order tensor, e.g., $\mathbf{A}:\mathbf{B}=A_{ijkl}B_{kl}$. The cross product of a second-order tensor $\mathbf{A}$ and a vector $\mathbf{V}$, the **div** and **curl** operations for second-order tensors are defined row by row, in analogy with the vectorial case. For any base vector $\mathbf{e}_i$ of the reference frame:

$$(\mathbf{A}\times\mathbf{V})^t\cdot\mathbf{e}_i=(\mathbf{A}^t\cdot\mathbf{e}_i)\times\mathbf{V} \tag{1}$$

$$(\mathbf{div}\,\mathbf{A})^t\cdot\mathbf{e}_i=\mathbf{div}\,(\mathbf{A}^t\cdot\mathbf{e}_i) \tag{2}$$

$$(\mathbf{curl}\,\mathbf{A})^t\cdot\mathbf{e}_i=\mathbf{curl}\,(\mathbf{A}^t\cdot\mathbf{e}_i). \tag{3}$$

In rectangular Cartesian components:

$$(\mathbf{A}\times\mathbf{V})_{ij}=e_{jkl}A_{ik}V_l \tag{4}$$

$$(\mathbf{div}\,\mathbf{A})_i=A_{ij,j} \tag{5}$$

$$(\mathbf{curl}\,\mathbf{A})_{ij}=e_{jkl}A_{il,k}. \tag{6}$$

where e_{jkl} is a component of the third-order alternating Levi–Civita tensor $\mathbf{X}$. A vector $\vec{\mathbf{A}}$ is associated with tensor $\mathbf{A}$ by using its trace inner product with tensor $\mathbf{X}$:

$$(\vec{\mathbf{A}})_k=-\frac{1}{2}(\mathbf{A}:\mathbf{X})_k=-\frac{1}{2}e_{ijk}A_{ij}. \tag{7}$$

In the component representation, the spatial derivative with respect to a Cartesian coordinate is indicated by a comma followed by the component index. A superposed dot represents a material time derivative.

2.2. Dislocations

In a continuum mechanics setting in the absence of fracture, the material displacement field vector $\mathbf{u}$ is defined continuously at any point of an elasto-plastic body. In the present paper, this is assumed to be true even at a resolution length scale below interatomic distances. Thus, the total distortion tensor, defined as the gradient of the displacement $\mathbf{U} = \mathbf{grad}\,\mathbf{u}$, is curl-free:

$$\mathbf{curl}\,\mathbf{U} = 0. \tag{8}$$

This equation is a necessary condition for the integrability of the displacement $\mathbf{u}$ and a compatibility condition for the distortion $\mathbf{U}$. Conversely it is sufficient to assure the existence of a single-valued continuous solution $\mathbf{u}$ to the equation $\mathbf{U} = \mathbf{grad}\,\mathbf{u}$, up to a constant translation.

In the elasto-plastic theory of dislocations, the plastic, $\mathbf{U_p}$, and elastic, $\mathbf{U_e}$, components of the distortion may not be compatible. Incompatible parts of the plastic and elastic distortion tensors, $\mathbf{U_p^\perp}$ and $\mathbf{U_e^\perp}$, which are not curl-free, may exist in the presence of dislocations, while additional curl-free compatible components, $\mathbf{U_e^\parallel}$ and $\mathbf{U_p^\parallel}$, allow satisfying the balance of equilibrium and boundary conditions. The following relations are therefore satisfied:

$$\mathbf{U} = \mathbf{U_e} + \mathbf{U_p} \tag{9}$$

$$\mathbf{U_e} = \mathbf{U_e^\perp} + \mathbf{U_e^\parallel} \tag{10}$$

$$\mathbf{U_p} = \mathbf{U_p^\perp} + \mathbf{U_p^\parallel} \tag{11}$$

$$0 = \mathbf{U_e^\perp} + \mathbf{U_p^\perp} \tag{12}$$

$$\mathbf{curl}\,\mathbf{U_e^\perp} = -\mathbf{curl}\,\mathbf{U_p^\perp} = \boldsymbol{\alpha} \neq 0. \tag{13}$$

The incompatibility equations (13) define the incompatible plastic distortion $\mathbf{U_p^\perp}$ associated with the presence of the Nye's dislocation density tensor $\boldsymbol{\alpha}$ (Nye, 1953), as well as the incompatible elastic distortion $\mathbf{U_e^\perp}$ offsetting the latter and ensuring the continuity of matter implied by Eq. (8). Since $\mathbf{U_e^\parallel}$ and $\mathbf{U_p^\parallel}$ are curl-free, Eq. (13) can also be written as:

$$\mathbf{curl}\,\mathbf{U_e} = -\mathbf{curl}\,\mathbf{U_p} = \boldsymbol{\alpha}. \tag{14}$$

Limiting ourselves to small deformations, one can define the strain tensor $\boldsymbol{\epsilon}$ as the symmetric part of the distortion $\mathbf{U}$, the rotation tensor $\boldsymbol{\omega}$ as its skew-symmetric part and the associated rotation vector $\vec{\boldsymbol{\omega}}$ as follows:

$$\vec{\boldsymbol{\omega}} = -\frac{1}{2}\boldsymbol{\omega} : \mathbf{X} = \frac{1}{2}\mathbf{curl}\,\mathbf{u}, \tag{15}$$

Using $\boldsymbol{\epsilon}$ and $\vec{\boldsymbol{\omega}}$, Eq. (8) becomes:

$$\mathbf{curl}\,\boldsymbol{\epsilon} + div(\vec{\boldsymbol{\omega}})\mathbf{I} - \mathbf{grad}^{\mathbf{t}}(\vec{\boldsymbol{\omega}}) = 0 \tag{16}$$

where $\mathbf{I}$ is the identity tensor. Transposing, then taking the **curl** of Eq. (16) leads to:

$$\mathbf{curl}\,\mathbf{curl}^{\mathbf{t}}(\boldsymbol{\epsilon}) = 0. \tag{17}$$

This relation is the classical Saint–Venant compatibility condition for the strain $\boldsymbol{\epsilon}$. It is a necessary condition for the integrability of the displacement $\mathbf{u}$. The trace of Eq. (16) similarly yields a compatibility condition for the rotation vector in the form:

$$div(\vec{\boldsymbol{\omega}}) = 0, \tag{18}$$

consistent with the curl nature of $\vec{\boldsymbol{\omega}}$. Applying the same curl-trace procedure to the elastic restriction of Eq. (14), we obtain from the curl operation, with self-evident notations, an equation parallel to Eq. (16):

$$\mathbf{curl}\,\boldsymbol{\epsilon}_e + div(\vec{\boldsymbol{\omega}}_e)\mathbf{I} - \mathbf{grad}^{\mathbf{t}}(\vec{\boldsymbol{\omega}}_e) = \boldsymbol{\alpha} \tag{19}$$

and a similar equation for the plastic restriction of Eq. (14):

$$\mathbf{curl}\,\boldsymbol{\epsilon}_p + div(\vec{\boldsymbol{\omega}}_p)\mathbf{I} - \mathbf{grad}^{\mathbf{t}}(\vec{\boldsymbol{\omega}}_p) = -\boldsymbol{\alpha}. \tag{20}$$

As elastic and plastic rotations, $(\vec{\boldsymbol{\omega}}_e, \vec{\boldsymbol{\omega}}_p)$ are integrable quantities. From the trace operation, we find an equation parallel to Eq. (18):

$$div(\vec{\boldsymbol{\omega}}_e) = -div(\vec{\boldsymbol{\omega}}_p) = \frac{1}{2}tr(\boldsymbol{\alpha}). \tag{21}$$

Motivated by the Saint–Venant compatibility condition (17), we transpose Eqs. (19, 20) further rearrange with the help of Eq. (21), to obtain:

$$\mathbf{grad}\,\vec{\boldsymbol{\omega}}_e = \mathbf{curl}^{\mathbf{t}}(\boldsymbol{\epsilon}_e) + \mathbf{K} \tag{22}$$

$$\mathbf{grad}\,\vec{\omega}_p = \mathbf{curl}^{\mathbf{t}}(\boldsymbol{\epsilon}_p) - \mathbf{K} \tag{23}$$

$$\mathbf{K} = \frac{1}{2} tr(\boldsymbol{\alpha})\mathbf{I} - \boldsymbol{\alpha}^t, \tag{24}$$

At this point, we can define the elastic, $\boldsymbol{\kappa}_e$, and plastic, $\boldsymbol{\kappa}_p$, curvature tensors as:

$$\boldsymbol{\kappa}_e = \mathbf{grad}\,\vec{\omega}_e \tag{25}$$

$$\boldsymbol{\kappa}_p = \mathbf{grad}\,\vec{\omega}_p \tag{26}$$

$$\mathbf{grad}\,\vec{\omega} = \boldsymbol{\kappa} = \boldsymbol{\kappa}_e + \boldsymbol{\kappa}_p \tag{27}$$

and take the **curl** of Eqs. (22, 23), to find:

$$\mathbf{curl}\,\boldsymbol{\kappa}_e = \mathbf{curl}\,\mathbf{curl}^{\mathbf{t}}(\boldsymbol{\epsilon}_e) + \mathbf{curl}\,\mathbf{K} = 0 \tag{28}$$

$$\mathbf{curl}\,\boldsymbol{\kappa}_p = \mathbf{curl}\,\mathbf{curl}^{\mathbf{t}}(\boldsymbol{\epsilon}_p) - \mathbf{curl}\,\mathbf{K} = 0 \tag{29}$$

Hence, in the elasto-plastic theory of dislocations, the elastic and plastic curvatures ($\boldsymbol{\kappa}_\mathbf{e}, \boldsymbol{\kappa}_\mathbf{p}$) are curl-free and, as mentioned above, the rotation vectors ($\vec{\omega}_e, \vec{\omega}_p$) are integrable single-valued quantities. **K** is Nye's curvature tensor (Nye, 1953), sometimes used to estimate the curvature tensors ($\boldsymbol{\kappa}_\mathbf{e}, \boldsymbol{\kappa}_\mathbf{p}$) by neglecting the contributions of the incompatible elastic and plastic strains. ($\boldsymbol{\kappa}_\mathbf{e}, \boldsymbol{\kappa}_\mathbf{p}$) are also known as the elastic and plastic bend-twist tensors, respectively.

2.3. Disclinations

As remarked by (deWit, 1970), ($\boldsymbol{\kappa}_\mathbf{e}, \boldsymbol{\kappa}_\mathbf{p}$) may not be curl-free anymore, if the possibility of multi-valued elastic and plastic rotations $\vec{\omega}_e$ and $\vec{\omega}_p$, *i.e.*, a discontinuity of the elastic and plastic rotations over some surface, is acknowledged. In such a situation, a non-zero tensor $\boldsymbol{\theta}$ such that

$$\boldsymbol{\theta} = -\mathbf{curl}\,\boldsymbol{\kappa}_\mathbf{p} = \mathbf{curl}\,\boldsymbol{\kappa}_\mathbf{e} \tag{30}$$

can be defined. $\boldsymbol{\theta}$ is the disclination density tensor, introduced by (deWit, 1970). Since the rotation vectors ($\vec{\omega}_e, \vec{\omega}_p$) are multi-valued in the present theory, the corresponding elastic and plastic rotation and distortion tensors are undefined. Substituting the elastic and plastic curvatures ($\boldsymbol{\kappa}_\mathbf{e}, \boldsymbol{\kappa}_\mathbf{p}$), which now include an incompatible part, for ($\mathbf{grad}\,\vec{\omega}_e, \mathbf{grad}\,\vec{\omega}_p$) in Eqs. (19, 20) leads to:

$$\mathbf{curl}\,\boldsymbol{\epsilon}_e = +\boldsymbol{\alpha} + \boldsymbol{\kappa}_e^t - tr(\boldsymbol{\kappa}_e)\mathbf{I} \tag{31}$$

$$\mathbf{curl}\,\boldsymbol{\epsilon}_p = -\boldsymbol{\alpha} + \boldsymbol{\kappa}_p^t - tr(\boldsymbol{\kappa}_p)\mathbf{I}. \tag{32}$$

Eqs. (31) and (32) relate elastic/plastic strain incompatibility arising from the presence of Nye's dislocation density tensor $\boldsymbol{\alpha}$ and elastic/plastic curvatures. They are modified forms of the incompatibility equations $\mathbf{curl}\,\mathbf{U_e} = -\mathbf{curl}\,\mathbf{U_p} = \boldsymbol{\alpha}$ considered in the elasto-plastic theory of dislocations (Acharya, 2001). In the compatible defect-free elastic theory ($\boldsymbol{\theta} = \mathbf{0}, \boldsymbol{\alpha} = \mathbf{0}$), the elastic displacement $\mathbf{u_e} = \mathbf{u}$ and rotation $\vec{\omega}_e = \vec{\omega}$ fields are continuous single-valued integrable fields. Then, it is only necessary to know the values of $\mathbf{u_e}$ and $\vec{\omega}_e$ at some particular point $\mathbf{r_0}$ to find their spatial dependence by integrating their gradients. Their expressions are (deWit, 1970):

$$\vec{\omega}_e(\mathbf{r}) = \vec{\omega}_e(\mathbf{r_0}) + \int_{\mathbf{r_0}}^{\mathbf{r}} \mathbf{d}\vec{\omega}_e(\mathbf{r}) = \vec{\omega}_e(\mathbf{r_0}) + \int_{\mathbf{r_0}}^{\mathbf{r}} \boldsymbol{\kappa}_e(\mathbf{r}) \cdot \mathbf{dr}, \tag{33}$$

$$\mathbf{u}_e(\mathbf{r}) = \mathbf{u}_e(\mathbf{r_0}) + \int_{\mathbf{r_0}}^{\mathbf{r}} \mathbf{du}_e(\mathbf{r}) = \mathbf{u}_e(\mathbf{r_0}) + \int_{\mathbf{r_0}}^{\mathbf{r}} \mathbf{U}_e(\mathbf{r}) \cdot \mathbf{dr}, \tag{34}$$

where **r** denotes a position vector. By decomposing the elastic distortion $\mathbf{U}_e$ into the elastic strain $\boldsymbol{\epsilon}_e$ and rotation $\boldsymbol{\omega}_e$, with the associated rotation vector $\vec{\omega}_e$, Eq. (34) can be rearranged into:

$$\mathbf{u}_e(\mathbf{r}) = \mathbf{u}_e(\mathbf{r_0}) + \int_{\mathbf{r_0}}^{\mathbf{r}} (\boldsymbol{\epsilon}_e(\mathbf{r}) + \boldsymbol{\omega}_e(\mathbf{r})) \cdot \mathbf{dr}, \tag{35}$$

$$\mathbf{u}_e(\mathbf{r}) = \mathbf{u}_e(\mathbf{r_0}) + \int_{\mathbf{r_0}}^{\mathbf{r}} (\boldsymbol{\epsilon}_e(\mathbf{r}) \cdot \mathbf{dr} + \vec{\omega}_e(\mathbf{r}) \times \mathbf{dr}), \tag{36}$$

$$\mathbf{u}_e(\mathbf{r}) = \mathbf{u}_e(\mathbf{r_0}) + \int_{\mathbf{r_0}}^{\mathbf{r}} (\boldsymbol{\epsilon}_e(\mathbf{r}) \cdot \mathbf{dr} + d(\vec{\omega}_e(\mathbf{r}) \times \mathbf{r}) - \mathbf{d}\vec{\omega}_e(\mathbf{r}) \times \mathbf{r}), \tag{37}$$

$$\mathbf{u}_e(\mathbf{r}) = \mathbf{u}_e(\mathbf{r_0}) + \vec{\omega}_e(\mathbf{r}) \times (\mathbf{r} - \mathbf{r_0}) + \int_{\mathbf{r_0}}^{\mathbf{r}} (\boldsymbol{\epsilon}_e(\mathbf{r}) - (\boldsymbol{\kappa}_e^t(\mathbf{r}) \times \mathbf{r})^t) \cdot \mathbf{dr}. \tag{38}$$

By integrating Eqs. (33) and (38) along a closed circuit C starting and finishing at point $\mathbf{r} = \mathbf{r_0}$ it is found:

$$[\vec{\omega}_e] = \int_{\mathbf{C}} \boldsymbol{\kappa}_e(\mathbf{r}) \cdot \mathbf{dr}, \tag{39}$$

$$[\mathbf{u}_e] = \int_{\mathbf{C}} (\boldsymbol{\epsilon}_e(\mathbf{r}) - (\boldsymbol{\kappa}_e^t(\mathbf{r}) \times \mathbf{r})^t) \cdot \mathbf{dr}, \tag{40}$$

where $[\vec{\omega}_e]$ and $[\mathbf{u}_e]$ denote a possible jump, *i.e.* a discontinuity, of the elastic rotation and displacement fields at $\mathbf{r_0}$. In the absence of defects, both $[\vec{\omega}_e]$ and $[\mathbf{u}_e]$ are zero, and the elastic rotation and displacement fields are single-valued. However, if the circuit C encompasses disclinations and dislocations, discontinuities arise. The discontinuity of the elastic rotation is the Frank vector and reads:

$$\boldsymbol{\Omega} = \int_C \boldsymbol{\kappa}_e \cdot \mathbf{dr}. \tag{41}$$

The discontinuity of the elastic displacement is the Burgers vector. It contains a possible contribution from the non-uniformity of elastic curvatures and reads (deWit, 1970):

$$\mathbf{b} = \int_C (\boldsymbol{\epsilon}_e - (\boldsymbol{\kappa}_e^t \times \mathbf{r})^t) \cdot \mathbf{dr}. \tag{42}$$

If S is the surface of unit normal $\mathbf{n}$ delimited by the circuit C, using Stokes' theorem and Eqs. (30, 31) allows rewriting Eqs. (41) and (42) as:

$$\boldsymbol{\Omega} = \int_S \mathbf{curl}\,(\boldsymbol{\kappa}_e) \cdot \mathbf{n} dS = \int_S \boldsymbol{\theta} \cdot \mathbf{n} dS, \tag{43}$$

$$\mathbf{b} = \int_S (\mathbf{curl}\,\boldsymbol{\epsilon}_e - (\mathbf{curl}\,(\boldsymbol{\kappa}_e) \times \mathbf{r})^t - \boldsymbol{\kappa}_e^t + tr(\boldsymbol{\kappa}_e)\mathbf{I}) \cdot \mathbf{n} dS, \tag{44}$$

$$\mathbf{b} = \int_S (\boldsymbol{\alpha} - (\boldsymbol{\theta} \times \mathbf{r})^t) \cdot \mathbf{n} dS. \tag{45}$$

$\boldsymbol{\Omega}$ and $\mathbf{b}$ defined above are point-wise measures of the lattice incompatibility in the presence of disclinations and dislocations. In contrast, the disclination and dislocation densities $\boldsymbol{\theta}$ and $\boldsymbol{\alpha}$ defined in Eqs. (30, 31) are continuous tensorial renditions of this incompatibility. They provide a natural regularization of the singular and discontinuous nature of the Frank/Burgers vectors.Importantly, as will be shown in Section 3.2, the contribution of disclinations to the overall Burgers vector in Eq. (45) leads to elastic constitutive laws containing internal length scales, which are specific to the elastic behavior in the core region of defects. Note that Eqs. (30, 31) may be utilized to estimate the disclination and Nye's dislocation density tensors from orientation maps provided by EBSD experiments, respectively (Beausir and Fressengeas, 2013).

2.4. Elasticity

An important consequence of Eq. (8) is that the material remains a continuum, capable of transmitting stresses and couple-stresses, at a resolution length scale below interatomic distances. As a consequence, the present theory accounts at this scale for internal stresses and couple-stresses due to the presence of dislocation and disclination densities (Taupin et al., 2013), through Eqs. (30) and (31). Moreover, stresses and couple-stresses remain bounded everywhere because defect density fields are used, rather than discrete defects leading to singularities. In the absence of body forces, the momentum and moment of momentum equations are:

$$\mathbf{div}\,\mathbf{T} = 0 \tag{46}$$

$$\mathbf{div}\,\mathbf{M} - \mathbf{T} : \mathbf{X} = 0, \tag{47}$$

where the stress tensor $\mathbf{T}$ is generally non-symmetric. Thus, the rotated stress vector $\mathbf{T} : \mathbf{X}$ balances the divergence of the couple-stress tensor $\mathbf{M}$ when $\mathbf{T}$ is non-symmetric. By taking the curl of Eq. (47) and eliminating the skew-symmetric part of the stress tensor from Eq. (46) and the latter, we can rewrite the above system (46, 47) as the higher order equilibrium equation (Mindlin and Tiersten, 1962; Taupin et al., 2013):

$$\mathbf{div}\mathbf{T}^{sym} + \frac{1}{2}\mathbf{curl}\,\mathbf{div}\,\mathbf{M}^{dev} = 0. \tag{48}$$

A specific free energy density function ψ containing contributions from elastic strains and curvatures is now introduced as follows:

$$\psi = \psi(\boldsymbol{\epsilon}_e, \boldsymbol{\kappa}_e), \tag{49}$$

and, following recent developments (Upadhyay et al., 2013), the elastic constitutive relations for the symmetric stress $\mathbf{T}^{sym}$ and deviatoric couple stress $\mathbf{M}^{dev}$ are chosen in the form:

$$\mathbf{T}^{sym} = \mathbf{C} : \boldsymbol{\epsilon}_e + \mathbf{D} : \boldsymbol{\kappa}_e \tag{50}$$

$$\mathbf{M}^{dev} = \mathbf{A} : \boldsymbol{\kappa}_e + \mathbf{B} : \boldsymbol{\epsilon}_e. \tag{51}$$

In view of Eqs. (15), (25) and (48) such a choice implies that the elastic rotation is readily eliminated from the elastic problem, whose sole unknown vector field is the elastic displacement $\mathbf{u_e}$. As a trade-off, the partial differential equations of the model involve second order derivatives of the elastic displacement components, in addition to the first order derivatives. As discussed (Upadhyay et al., 2013), the elasticity tensors $\mathbf{B}$ and $\mathbf{D}$ vanish in isotropic and centro-symmetric media. However, centro-symmetry is broken in the presence of crystal defects (dislocations and disclinations), which yields non-zero $\mathbf{B}$ and $\mathbf{D}$ tensors. A central issue in the present work lies in the connections existing between the $\mathbf{A}, \mathbf{B}$ and $\mathbf{D}$ elasticity tensors and the characteristic length scales of the defected areas. This issue will be treated and a justification will be offered for Eqs. (50) and (51) below in Section 3.2.

2.5. Plasticity

In the presence of stress and couple-stress fields, the dislocation and disclination densities may be set into motion with respective velocities $\mathbf{V}_\alpha$ and $\mathbf{V}_\theta$. The evolution of the disclination density follow the transport equation derived (Fressengeas et al., 2011):

$$\dot{\boldsymbol{\theta}} = -\mathbf{curl}\,(\boldsymbol{\theta} \times \mathbf{V}_\theta). \tag{52}$$

By comparing the above equation with the time derivative of Eq. (30), the plastic curvature rate tensor can be identified as:

$$\dot{\boldsymbol{\kappa}}_p = \boldsymbol{\theta} \times \mathbf{V}_\theta, \tag{53}$$

where no extra gradient term is needed in the absence of any additional inelastic curvature rate. Similarly, the transport equation for the dislocation density is (Fressengeas et al., 2011):

$$\dot{\boldsymbol{\alpha}} = -\mathbf{curl}\,\dot{\boldsymbol{\epsilon}}_p + \dot{\boldsymbol{\kappa}}_p^t - tr(\dot{\boldsymbol{\kappa}}_p)\mathbf{I} = -\mathbf{curl}\,\dot{\boldsymbol{\epsilon}}_p + \mathbf{s}_\theta, \tag{54}$$

where the plastic strain rate $\dot{\boldsymbol{\epsilon}}_p$ is:

$$\dot{\boldsymbol{\epsilon}}_p = \frac{1}{2}(\boldsymbol{\alpha} \times \mathbf{V}_\alpha + (\boldsymbol{\alpha} \times \mathbf{V}_\alpha)^t). \tag{55}$$

A remarkable feature of Eq. (54) is that dislocations are nucleated not only through the incompatibility of the plastic strain rate, but also by the source term $\mathbf{s}_\theta = \dot{\boldsymbol{\kappa}}_p^t - tr(\dot{\boldsymbol{\kappa}}_p)\mathbf{I}$, which arises from the mobility of the disclinations. The meaning of this source term is that a wake of nucleated or annihilated dislocations accompanies the motion of disclinations. As will be shown in Section 3.3, this source mechanism is central to the production of shear-coupled boundary migration.

The Peach–Köhler-type driving forces $\mathbf{F}_\alpha$ and $\mathbf{F}_\theta$ acting on disclination and dislocation densities are chosen on a thermodynamical basis, by ensuring that the power dissipation due to defect mobility is non-negative (Fressengeas et al., 2011). For the sake of simplicity, linear viscosity is assumed, restricting our simulations to sufficiently moderate temperatures (or large strain rates). Of course, more sophisticated constitutive laws could be adopted to reflect thermally assisted obstacle overcoming. Hence, the dislocation and disclination velocities read:

$$V_l^\alpha = \frac{1}{B_\alpha} e_{jkl} \frac{T_{ij} + T_{ji}}{2} \alpha_{ik} \tag{56}$$

$$V_l^\theta = \frac{1}{B_\theta} e_{jkl} M_{ij} \theta_{ik}, \tag{57}$$

where B_α and B_θ are positive drag coefficients. These coefficients will be further discussed below in Section 2.6.

2.6. Two-dimensional edge-wedge model

For completeness, we now briefly recall the two-dimensional edge-wedge model (Fressengeas et al., 2011; Taupin et al., 2013) used in the forthcoming simulations. We limit the fields of crystal defects envisioned to uniaxial distributions of wedge disclinations, which is sufficient for the interpretation of symmetric tilt boundaries. Thus, we assume the disclination tensor to be: $\boldsymbol{\theta} = \theta_{33}\mathbf{e_3} \otimes \mathbf{e_3}$ in the orthonormal reference frame $(\mathbf{e_1}, \mathbf{e_2}, \mathbf{e_3})$, all other components being zero. The continuity condition $\mathbf{div}\boldsymbol{\theta} = 0$ is $\theta_{33,3} = 0$, implying that θ_{33} depends only on the coordinates $(x_1, x_2) : \theta_{33} = \theta_{33}(x_1, x_2)$. In component form, the rotational incompatibility Eq. (30) reads: $\theta_{ij} = -e_{jkl}\kappa_{il,k}^p = e_{jkl}\kappa_{il,k}^e$. In the present case, it reduces to:

$$\theta_{33} = \kappa_{31,2}^p - \kappa_{32,1}^p = \kappa_{32,1}^e - \kappa_{31,2}^e. \tag{58}$$

Hence the only relevant elastic and plastic curvatures are: $(\kappa_{31}^e, \kappa_{32}^e)$ and $(\kappa_{31}^p, \kappa_{32}^p)$. Additionally, we note that: $tr(\boldsymbol{\kappa}_p) = 0$. Thus, the disclination transport Eq. (52) is:

$$\dot{\theta}_{33} = \dot{\kappa}_{31,2}^p - \dot{\kappa}_{32,1}^p. \tag{59}$$

The plastic curvature rate (53) reads, in component form: $\dot{\kappa}_{ij}^p = e_{jkl}\theta_{ik}V_l^\theta$. Hence, we find:

$$\dot{\kappa}^p_{31} = -\theta_{33} V^\theta_2 \tag{60}$$

$$\dot{\kappa}^p_{32} = +\theta_{33} V^\theta_1. \tag{61}$$

Using the constitutive relation (57) for the disclination velocities provides their relationship with the couple-stresses:

$$V^\theta_1 = +\frac{1}{B_\theta} M_{32}\theta_{33} \tag{62}$$

$$V^\theta_2 = -\frac{1}{B_\theta} M_{31}\theta_{33}. \tag{63}$$

Using Eq. (55), it is seen that the motion of the dislocations produces the plastic strain rate components $(\dot{\epsilon}^p_{11}, \dot{\epsilon}^p_{12}, \dot{\epsilon}^p_{21}, \dot{\epsilon}^p_{22})$:

$$\dot{\epsilon}^p_{11} = -\alpha_{13} V^\alpha_2 \tag{64}$$

$$\dot{\epsilon}^p_{12} = \dot{\epsilon}^p_{21} = \frac{1}{2}(\alpha_{13} V^\alpha_1 - \alpha_{23} V^\alpha_2) \tag{65}$$

$$\dot{\epsilon}^p_{22} = +\alpha_{23} V^\alpha_1. \tag{66}$$

The above relations suggest that out-of-plane motion of the edge dislocations $(\alpha_{13}, \alpha_{23})$ is involved in the extension rates $(\dot{\epsilon}^p_{11}, \dot{\epsilon}^p_{22})$, whereas their glide is responsible for $\dot{\epsilon}^p_{12}$. Consistently, the dislocation transport Eq. (54) reduces to:

$$\dot{\alpha}_{13} = \dot{\epsilon}^p_{11,2} - \dot{\epsilon}^p_{12,1} + \dot{\kappa}^p_{31} \tag{67}$$

$$\dot{\alpha}_{23} = \dot{\epsilon}^p_{21,2} - \dot{\epsilon}^p_{22,1} + \dot{\kappa}^p_{32}. \tag{68}$$

Since the trace of the plastic curvature rate tensor is zero, the source $\mathbf{s}_\theta$ in the dislocation transport Eq. (54) generates only edge dislocations densities $(\alpha_{13}, \alpha_{23})$. Thus, if all other dislocation densities are initially absent, the dislocation distribution involves only α_{13} and α_{23} edge densities. The symmetric "Peach–Köhler" constitutive relationship (56) provides the dislocation velocities in terms of the stress tensor, for both the out-of-plane motion of dislocations (*e.g.* climb, cross-slip or diffusion):

$$V^\alpha_1 = +\frac{1}{B^c_\alpha} T_{22}\alpha_{23} \tag{69}$$

$$V^\alpha_2 = -\frac{1}{B^c_\alpha} T_{11}\alpha_{13}, \tag{70}$$

and their glide:

$$V^\alpha_1 = +\frac{1}{2B^g_\alpha}(T_{12} + T_{21})\alpha_{13} \tag{71}$$

$$V^\alpha_2 = -\frac{1}{2B^g_\alpha}(T_{12} + T_{21})\alpha_{23}. \tag{72}$$

In forthcoming simulations, the contributions to plasticity of glide and out-of-plane motion of dislocations are weighed through the drag coefficient ratio $\eta = B^g_\alpha / B^c_\alpha$, taken to be $\eta = 0.1$. Diffusive motion of dislocations is then made ten times more difficult than dislocation glide. The value $\eta = 1$ will also be tentatively used below to check for the possible influence of climb on shear-coupled boundary migration at high temperatures. Of course, a thorough account of temperature effects on diffusive mechanisms would lead to a more elaborate dependence. Further, disclination drag is supposed to be of the order of dislocation drag: $B_\theta = B^g_\alpha = B$.

3. Simulations of shear-coupled migration of tilt boundaries

3.1. From atomistic to continuous modeling of tilt boundaries

For convenience, we now shortly recall the construction method developed (Fressengeas et al., 2013) to model ⟨001⟩ tilt boundaries in copper bicrystals. This method aims at establishing a crossover between a discrete atomistic grain boundary configuration and an equivalent continuous disclination density field at the same scale. The methodology is shown in Figs. (1) and (2) for Σ13(510) and Σ5(310) boundaries of misorientation 22.62° and 36.87°, respectively.

To generate a symmetric tilt boundary in atomistic simulations, two adjacent crystals are first separately rotated about the ⟨001⟩ axis threading the plane at the coincidence site lattice (CSL) point C1, the bottom crystal (red atoms in the figure) by an angle $-\theta/2$ and the top crystal (black atoms) by the angle $+\theta/2$. Thus an overlapping triangle C1QR is generated, where full/empty red/black circles correspond to atoms belonging to two consecutive atomic planes parallel to the figure in both crystals. In this overlapping area, and by periodicity in all similar areas along the grain boundary, extra-atoms need to be removed to minimize the incompatibility of the resulting bicrystal. As there is no recipe in selecting the removed atoms, a trial and error procedure must be used to infer the atomistic configuration involving minimum energy after subsequent relaxation. We now imagine an analogous "cut, symmetrically distort and glue" procedure in the continuous setting. The

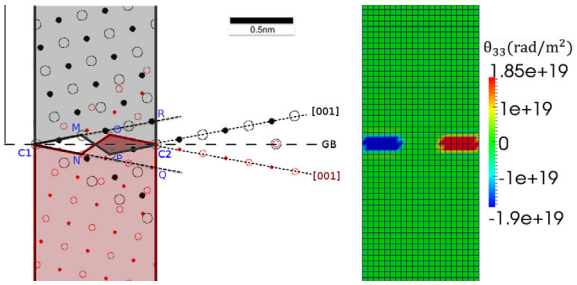

Fig. 1. Method of construction of a bicrystal featuring a $\Sigma 13(510)$ symmetric $\langle 001 \rangle$ tilt boundary of misorientation 22.62°. Left: Identification by atomic positions of negative and positive material wedges C1MN and C2OP necessary to accommodate the incompatibility between the two crystals. Right: Equivalent wedge disclination density θ_{33} (rad/m^2) used in the simulations.

top and bottom crystals are now seen as continua sketched by red and black filling colors in Figs. 1 and 2. After rotating these two crystals, wedge-shaped pieces of superimposed material may be removed or retained in the overlapping areas in order to accommodate the incompatibility. Cuts are made to define these wedges according to the position of atoms that need to be removed or retained to minimize incompatibility in the atomistic configuration. The cuts start and finish at the CSL points C1 and C2, where there is no incompatibility, and extend along the paths C1NOC2 and C1MPC2 in the bottom and top crystals, respectively. For the $\Sigma 13(510)$ boundary shown in Fig. 1, the triangle C1MN corresponds to a negative wedge and the triangle C2OP to a positive wedge in both continua. These wedges have opposite signs for the $\Sigma 5(310)$ boundary shown in Fig. 2. Next, the new edges (C1M, C1N), (C2O, C2P) and (MP, NO) are distorted (rotated and deformed), merged and glued to ensure continuity of matter. In the process, the top and bottom continua are symmetrically distorted to fill the negative wedge and to eliminate overlapping in the positive wedge. The resulting bicrystal contains a wedge disclination dipole accommodating the material incompatibility between the CSL points C1 and C2. The positive wedge tends to open the material, while the negative one tends to close it down. Note that the separation distance (MP,NO) of the dipole must be small to account for the elastic energy of the boundary. Thus this construction is limited to low Σ boundaries but is sufficient for the present purpose, which consists in showing the capabilities of our theory at smoothly modeling shear-coupled boundary migration. As a final step to this transition from atomistic to continuous description of the grain boundary, a disclination density value: the opening angle θ of the wedges per unit square, is ascribed to the nodes of the finite element mesh lying along the projections of the edges C1M and C2O on the boundary. The resulting field, shown in Figs. 1 and 2 for an element size of approximately 0.05 nm, is used in the following as the initial disclination configuration in relaxation simulations, where the disclinations are allowed to move and relax in their own stress and couple stress fields until the overall elastic energy stabilizes. Periodic boundary conditions are used on vertical boundaries. The validation of our tilt boundary construction method was provided (Fressengeas et al., 2013), where it was shown in particular that the core energy of symmetric tilt boundaries is naturally retrieved by the theory without any ad hoc fitting parameter. As can be seen by comparing Figs. 1 and 2, a remarkable feature emerges from our construction method. In the $[0°, 36.87°[$ misorientation range, the polarity of the wedge dipole is $\langle -+ \rangle$ from left to right, while the wedge angle θ separates the [001] directions of the two crystals. In the $[36.87°, 90°]$ range, the polarity is opposite, and it is now the [110] orientation axes of the two crystals that are separated

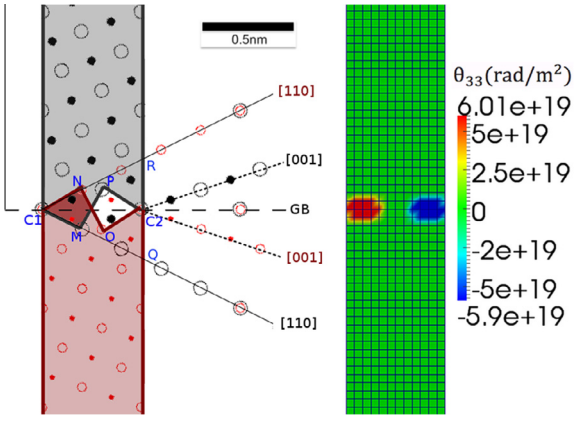

Fig. 2. Method of construction of a bicrystal featuring a $\Sigma 5(310)$ symmetric $\langle 001 \rangle$ tilt boundary of misorientation 36.87°. Left: Identification by atomic positions of positive and negative material wedges C1MN and C2OP necessary to accommodate the incompatibility between the two crystals. Right: Equivalent wedge disclination density θ_{33} (rad/m^2) used in the simulations.

by the wedge angle. This sharp change of polarity around 37° is in strong analogy with the ⟨001⟩ and ⟨110⟩ shear deformation modes identified (Cahn et al., 2006). This crossover will be thoroughly discussed in Section 3.5 below.

3.2. Core elastic constitutive laws

In this Section, we focus on describing the elastic properties of a defected solid, particularly in the defect core region. The discussion is limited to the present edge-wedge model, where the only relevant stress and couple-stress components are $(T_{11}, T_{12}, T_{21}, T_{22})$ and (M_{31}, M_{32}) respectively. The dimension of the elastic constants in the fourth-order tensors $\mathbf{C}$, $(\mathbf{B}, \mathbf{D})$ and $\mathbf{A}$ in Eqs. (50, 51) are respectively that of stress, stress × length and stress × length^2. Assuming cubic symmetry of the crystal, the relations $C_{1111} = C_{2222}, C_{1122} = C_{2211}, C_{1221} = C_{1212} = C_{2112} = C_{2121}$ hold between the components of the elastic tensor $\mathbf{C}$ in Eq. (50). The elastic tensor $\mathbf{A}$ induces couple-stresses in the defected regions of the crystals, because the symmetry of the stress tensor is broken by the fluctuations of the atomic interactions. As already mentioned both $\mathbf{B}$ and $\mathbf{D}$ are zero in isotropic, centro-symmetric media. However, centro-symmetry is broken in the presence of crystal defects, which yields non zero $\mathbf{B}$ and $\mathbf{D}$ tensors (Upadhyay et al., 2013). Due to tensor $\mathbf{D}$, the strong fluctuations of the elastic rotation over the defect core region induce stresses, whereas the tensor $\mathbf{B}$ gives rise to couple stresses following from the fluctuations in strain in this region. In the present "edge-wedge" model, the infinitesimal displacement $\mathbf{du} = (\boldsymbol{\kappa}_e^t \times \mathbf{r})^t.\mathbf{dr}$ arising from an inhomogeneity of the lattice curvatures $(\kappa_{31}^e, \kappa_{32}^e)$ over the vector $\mathbf{r} = (r_1, r_2)$ in some domain $\mathcal{D}$ of the defected area is, in component form:

$$du_1 = -\kappa_{31}^e r_2 dr_1 - \kappa_{32}^e r_2 dr_2 = \epsilon'_{11} dr_1 + \epsilon'_{12} dr_2 \tag{73}$$
$$du_2 = +\kappa_{31}^e r_1 dr_1 + \kappa_{32}^e r_1 dr_2 = \epsilon'_{21} dr_1 + \epsilon'_{22} dr_2. \tag{74}$$

Thus, for example, the tensile stress T_{11}^{sym} is:

$$T_{11}^{sym} = C_{1111}\left(\epsilon_{11}^e + \frac{1}{V_{\mathcal{D}}}\int_{\mathcal{D}} \epsilon'_{11} dv\right) + C_{1122}\left(\epsilon_{22}^e + \frac{1}{V_{\mathcal{D}}}\int_{\mathcal{D}} \epsilon'_{22} dv\right) \tag{75}$$
$$T_{11}^{sym} = C_{1111}\left(\epsilon_{11}^e - \frac{1}{V_{\mathcal{D}}}\int_{\mathcal{D}} r_2 \kappa_{31}^e dv\right) + C_{1122}\left(\epsilon_{22}^e + \frac{1}{V_{\mathcal{D}}}\int_{\mathcal{D}} r_1 \kappa_{32}^e dv\right), \tag{76}$$

where $V_{\mathcal{D}}$ is the volume of domain $\mathcal{D}$. To avoid an integral formulation over $\mathcal{D}$, we cast this nonlocal dependence of the stress into the averaged form:

$$T_{11}^{sym} = C_{1111}\epsilon_{11}^e + C_{1122}\epsilon_{22}^e - C_{1111}\bar{r}_2 \kappa_{31}^e(\bar{\mathbf{r}}) + C_{1122}\bar{r}_1 \kappa_{32}^e(\bar{\mathbf{r}}), \tag{77}$$

where $\bar{\mathbf{r}}$ is some point in domain $\mathcal{D}$, which justifies constitutive relations in the form of Eq. (50) or, in this two-dimensional setting:

$$T_{11}^{sym} = C_{1111}\epsilon_{11}^e + C_{1122}\epsilon_{22}^e - D_{1131}\kappa_{31}^e + D_{1132}\kappa_{32}^e \tag{78}$$
$$T_{12}^{sym} = C_{1212}\epsilon_{12}^e + C_{1221}\epsilon_{21}^e + D_{1231}\kappa_{31}^e - D_{1232}\kappa_{32}^e \tag{79}$$
$$T_{21}^{sym} = C_{2112}\epsilon_{12}^e + C_{2121}\epsilon_{21}^e + D_{2131}\kappa_{31}^e - D_{2132}\kappa_{32}^e \tag{80}$$
$$T_{22}^{sym} = C_{2211}\epsilon_{11}^e + C_{2222}\epsilon_{22}^e - D_{2231}\kappa_{31}^e + D_{2232}\kappa_{32}^e, \tag{81}$$

where the averaged curvatures are approximated by their values at the point of interest and the D_{ijkl} elastic constants reflect the size of domain $\mathcal{D}$ in the core region. Similarly, the infinitesimal rotation $\mathbf{d\omega} = \mathbf{r} \times \boldsymbol{\epsilon}_e.\mathbf{dr}/r^2$ induced by the inhomogeneity of the in-plane strains $(\epsilon_{21}^e, \epsilon_{22}^e)$ and $(\epsilon_{11}^e, \epsilon_{12}^e)$ over the core region produce curvature components $(\kappa'_{31}, \kappa'_{32})$ respectively

$$d\omega_3 = \frac{1}{r^2}(r_1\epsilon_{21}^e - r_2\epsilon_{11}^e)dr_1 + \frac{1}{r^2}(r_1\epsilon_{22}^e - r_2\epsilon_{12}^e)dr_2 = \kappa'_{31}dr_1 + \kappa'_{32}dr_2 \tag{82}$$

giving rise in turn, in average over a domain $\mathcal{D}$ of the core region, to couple-stress components (M_{31}, M_{32}). We therefore conjecture that Eq. (51) takes the form:

$$M_{31}^{dev} = A_{3131}\kappa_{31}^e - B_{3111}\epsilon_{11}^e + B_{3112}\epsilon_{12}^e + B_{3121}\epsilon_{21}^e \tag{83}$$
$$M_{32}^{dev} = A_{3232}\kappa_{32}^e - B_{3212}\epsilon_{12}^e - B_{3221}\epsilon_{21}^e + B_{3222}\epsilon_{22}^e, \tag{84}$$

where the B_{ijkl} elastic constants reflect the size of domain $\mathcal{D}$ in the core region. Hence, $\mathbf{B}$ and $\mathbf{D}$ characterize nonlocal elastic behavior in the defected crystal. From the results (Upadhyay et al., 2013), the symmetry $B_{ijkl} = D_{klij}$ of the elasticities must hold. Thus, for example, $D_{1131} = B_{3111}$, which we may write, using Eqs. (73, 82): $-D'_{1131}r_2 = -B'_{3111}/r^2$. Therefore: $B'_{3111}/D'_{1131} = r^2$. The same value r^2 is obtained for all B'_{ijkl}/D'_{klij} ratios. The distance r is the internal length scale that sets the characteristic dimension of the area over which inhomogeneity of the elastic curvatures/strains induces a significant stress/couple stress component. Following estimates provided (Maranganti and Sharma, 2007), it is given the value $r = 0.5$ Åto limit this area to the core region of the defects. Hence, the simplest choice for the non-zero components of the elasticity tensors $(\mathbf{A}, \mathbf{B}, \mathbf{D})$ is $A_{ijkl} = \mu r^2, B_{ijkl} = D_{klij} = \mu r$. The parameter values used for copper are presented in Table 1. We note from Fig. 1 that, not surprisingly, $r = 0.5$ Å is in line with the length of the segments $C1M = C1N$ providing a measure of the extent of the wedge disclination core.

Table 1
Numerical constants used in the model.

b	C_{1212}	C_{1111}	C_{1122}	b^2B	l
0.286 nm	27 GPa	175 GPa	125 GPa	10^4 Pa.s	0.05 nm

In the present context of shear-coupled boundary migration, a fundamental consequence of the nonlocal elastic constitutive laws is that elastic shear strains generate couple-stresses, which sets disclinations into motion according to Eqs. (57), (62) and (63), and that elastic curvatures generate stresses, which sets dislocations into motion according to Eqs. (56), (69)–(71) and (72). In particular, the elastic constant B_{3112} induces the couple-stress M_{31} under the shear strain ϵ_{12}, which leads to motion normal to the grain boundary of the θ_{33} wedge-disclination dipoles (see Eq. (63)). As a result of this disclination motion, α_{13} edge dislocation density is nucleated according to Eqs. (60) and (67) (possibly with partial Burgers vector), and the latter moves by glide along the grain boundary, according to Eq. (71). It may be of interest to contrast this situation with, say, tensile loading normal to the boundary. Then, the tensile strain ϵ_{22} generates the couple-stress M_{32} through the term B_{3222}, then leads to the motion of θ_{33} disclinations along the grain boundary (see Eq. 62), in agreement with other modeling approaches (Gutkin et al., 2003). In this motion, α_{23} edge dislocation density is nucleated, according to Eqs. (61) and (68), and this density moves by climb along the boundary, according to Eq. (69). Diffusion processes are then clearly involved in the deformation of the grain boundary.

3.3. Kinematics of shear-coupled boundary migration

Let us now illustrate shear-coupled boundary migration at moderate temperature by applying a positive shear strain to a copper bicrystal containing a $\Sigma5(310)$ symmetric $\langle001\rangle$ tilt boundary of misorientation 36.87°, as shown in Fig. 3. As a result, the wedge disclination array moves downward in the figure. As discussed above, this motion generates edge dislocation density α_{13}, with line direction normal to the figure and Burgers vector along the boundary. Positive partial Burgers vectors arise from the motion of positive disclinations and vice versa. Thus, the motion of the disclination dipoles creates dislocation density dipoles. Under shear loading, the dislocation density dipoles glide along the boundary and annihilate at mid-distance, as can be seen by comparing Fig. 3(a) and (b). Remarkably, the disclination dipole structure of the tilt boundary is preserved in this dislocation emission/glide/annihilation mechanism. The involved dislocation glide produces the positive plastic shear strain field shown in Fig. 4(a). Meanwhile the plastic rotation field shown in Fig. 4(b) is generated by the normal motion of the disclination dipoles, *i.e.* by tilt boundary migration. This decomposition of the mechanism has similarities with those proposed on a geometrical basis (Cahn et al., 2006) and (Khater et al., 2012) in the framework of disconnections. Good agreement is also obtained between the heterogeneity at interatomic scale of the plastic shear strain/plastic rotation fields shown in Fig. 4 and the shear strain gradient/micro-rotation fields post-processed from atomistic simulations (Zimmerman et al., 2009; Tucker et al., 2010; Tucker et al., 2012) (see Figs. 3(a) and 6(a) in reference (Tucker et al., 2010)). Perhaps unexpectedly, our predicted shear strain field is even more heterogeneous than that obtained from the atomistic simulations. Note in Fig. 4 that large plastic strains are generated. This suggests that the present theory should be written in a finite strain setting. However, despite this shortcoming, the present theory keeps its ability at reproducing the kinematics of shear-coupled boundary migration, and shows excellent agreement with atomistic simulations and experiments. Since the boundary migrates downward and positive shear is produced, the shear coupling factor is negative. As aforementioned, its value is estimated by the

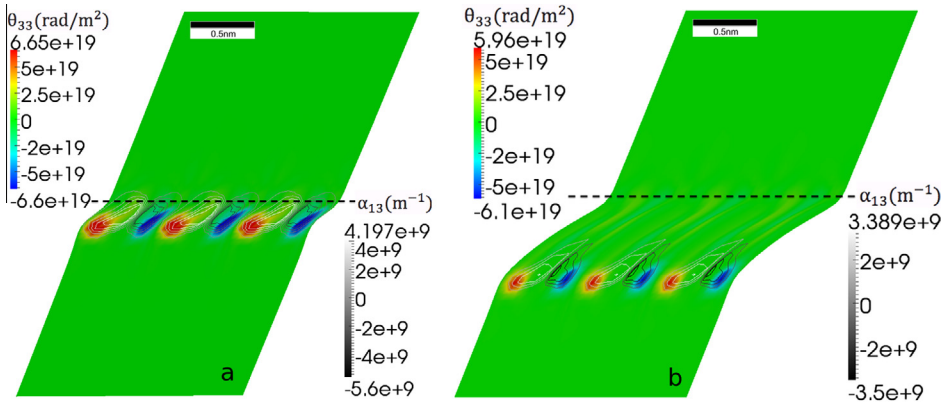

Fig. 3. Wedge disclination density θ_{33} (rad/m^2) (color coded) and edge dislocation density α_{13} (m^{-1}) (black/white contours), representing the migration of a $\Sigma5(310)$ symmetric $\langle001\rangle$ tilt grain boundary of misorientation 36.87°. Two snapshots are taken after a time of approximately 1 ms (a) and 10 ms (b). A macroscopic shear strain of +0.2 is applied. The black dashed-line indicates the initial position of the wedge disclination dipoles.

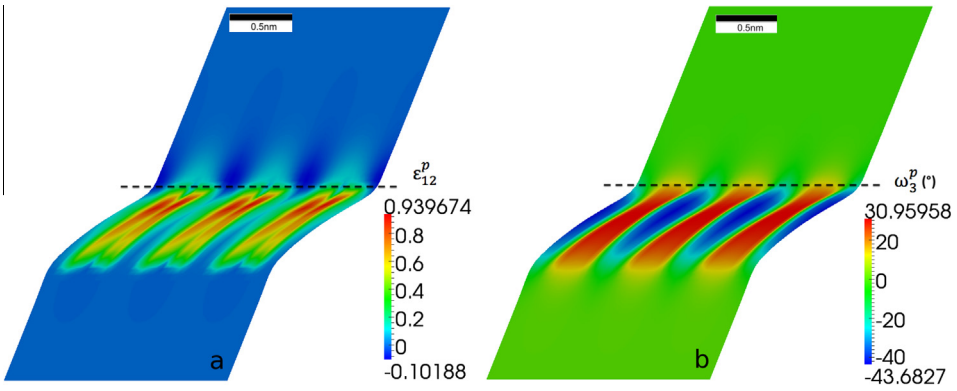

Fig. 4. Plastic shear strain ϵ_{12}^p (a) and plastic rigid body rotation $\omega_3^p(^\circ)$ (b), after the migration of a $\Sigma5(310)$ symmetric $\langle 001\rangle$ tilt grain boundary of misorientation 36.87°. These snapshots are taken after a time of approximately 10 ms, corresponding to the position of wedge disclination dipoles shown in Fig. 3(b). The black dashed-line indicates the initial position of the wedge disclination dipoles.

ratio of the relative parallel translation of the two crystals by the normal migration of the grain boundary, $\beta = u_{//}/u_{\perp}$. The value $\beta \approx -0.94$ is in good agreement with atomistic simulations and experiments (Cahn et al., 2006; Gorkaya et al., 2009).

3.4. Reversibility, dislocation climb

In Fig. 5, we additionally show the reversibility of the boundary migration when shear loading is reversed, in good agreement with atomistics simulations (Cahn et al., 2006). The influence of climb on this mechanism is now investigated by setting the climb-to-glide drag ratio to $\eta = 1$ to mimicking a temperature increase, which implies that the climb of dislocations is made as easy as dislocation glide. The resulting plastic shear and disclination density fields are shown in Fig. 6(a)–(c) in comparison with prevailing dislocation glide conditions in Fig. 6(b) and (c). It is seen that the dislocation dipoles follow more closely the migration of the disclination dipoles and that the heterogeneity of the plastic shear field is milder.Further, the shear coupling parameter shifts from $\beta \approx -0.94$ to $\beta \approx -0.82$, indicating less efficient plastic shear production of the migration process.

3.5. Shear-coupling factor

As aforementioned, the polarity of the wedge disclination dipoles is $\langle -+\rangle$ in the range of misorientations $[0^\circ, 36.87^\circ[$, while the wedge angle is the orientation difference between [001] directions in the two crystals, whereas in the range $[36.87^\circ, 90^\circ]$, the polarity is opposite and the wedge angle is the orientation gap between [110] directions. Thus, all [001]-type tilt boundaries migrate upward in the range $[0^\circ, 36.87^\circ[$, while all [110]-type boundaries migrate downward in the range $[36.87^\circ, 90^\circ]$. As an example, the shear-coupled migration of a $\Sigma13(510)$ symmetric $\langle 001\rangle$ tilt boundary of misorientation 22.62° is now shown in Fig. 7. The shear coupling factor is $\beta \approx 0.42$ and its variations in the complete misorientation range are shown in Fig. 8. It is seen that the $\langle 001\rangle$ and $\langle 110\rangle$ branches obtained by molecular dynamics simulations and by experiments (Cahn et al., 2006; Gorkaya et al., 2009) are retrieved. This result is a natural outcome of the procedure introduced in Section 3.1 to derive wedge disclination dipoles from atomistic structures. It is also in agreement with predictions of surface-dislocation-based models (Cahn et al., 2006; Berbenni et al., 2013), where the shear coupling factor depends on the dislocation content of the boundary. However, it must be considered as only formally correct in these models because they are actually restricted to low-angle boundaries to prevent dislocation core overlapping. It is fully consistent in the present

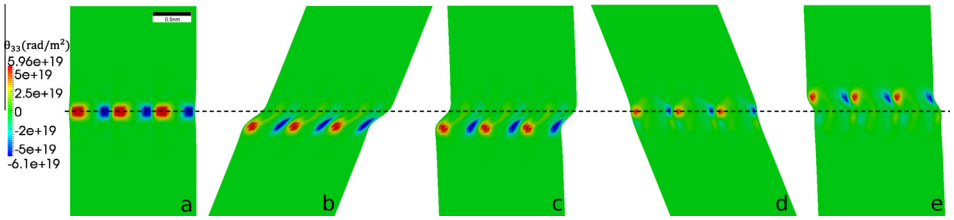

Fig. 5. Snaphots of the wedge disclination density θ_{33} ;(rad/m^2) during the reversible migration of a $\Sigma5(310)$ symmetric $\langle 001\rangle$ tilt grain boundary of misorientation 36.87°. (a): Initial grain boundary; (b): during applied positive shear after approximately 3 ms; (c): when unloading the sample; (d): during applied negative shear after approximately 3 ms; (e): after unloading the sample. The dashed-line indicates the initial position of the wedge disclination dipoles in (a).

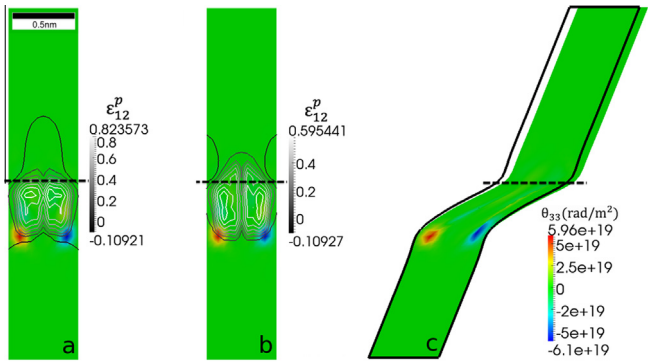

Fig. 6. Wedge disclination density θ_{33} (rad/m^2) (color coded) and plastic shear ϵ_{12}^p (black/white contours), representing the migration of a $\Sigma5(310)$ symmetric $\langle 001\rangle$ tilt grain boundary of misorientation 36.87°. A macroscopic shear strain of +0.2 is applied. A single disclination dipole is shown. Snapshots taken after a time of approximately 10 ms, (a,c): for prevailing glide $\eta = 0.1$; b: for easy climb $\eta = 1$. In (c), color-coded is shown the final position of the sample in the easy glide condition. The thick black line indicates the final position of the sample in easy climb conditions, indicating less efficient plastic shear production of the migration process. The black dashed-line indicates the initial position of the disclination dipole.

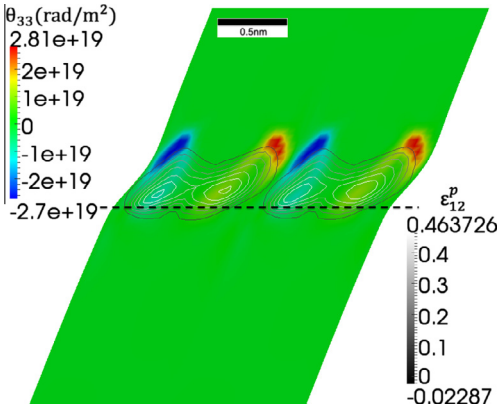

Fig. 7. Wedge disclination density θ_{33} (rad/m^2) (color coded) and plastic shear strain ϵ_{12}^p (black/white contours), representing the migration of a $\Sigma13(510)$ symmetric $\langle 001\rangle$ tilt grain boundary of misorientation 22.62°. This snapshot is taken after a time of approximately 10 ms, a macroscopic shear strain of +0.2 is applied. The black dashed-line indicates the initial position of the wedge disclination dipoles.

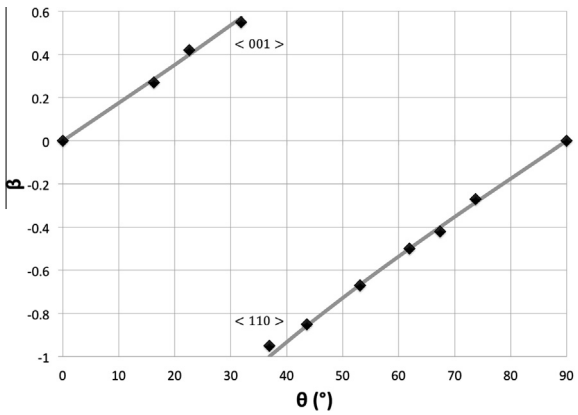

Fig. 8. Shear-coupling factor as a function of misorientation. The dots represent the values obtained by the present simulations. The two solid lines represent the values predicted by the $\langle 001\rangle$ and $\langle 110\rangle$ shear deformation modes defined (Cahn et al., 2006).

disclination-based approach, because the latter is also appropriate at high-angles where it leads to the correct core energy of the boundaries.

4. Conclusions

The elasto-plastic theory of crystal defect fields (disclinations and dislocations) (Fressengeas et al., 2011) was used to describe in a continuous manner the shear-coupled migration of symmetric $\langle 001 \rangle$ tilt boundaries in copper. In the dynamic simulations, the initial configuration of the boundaries was built from wedge-disclination dipole arrays defined after their atomistic topography. Lattice symmetry breaking in the boundary area is at the origin of specific core elastic constitutive laws, which contain an internal length scale identified from the atomistic topography of the boundary. Its very small value, about 0.5 Å, implies that nonlocal elasticity is limited to the defects core region and disappears away from it, in agreement with previous findings (Upadhyay et al., 2013). By ensuring the presence of couple stresses in the defected area in simple shear loading, nonlocal elasticity plays a central role in securing a driving force for the motion of the disclination dipoles. It is only in its presence that boundary migration driven by simple shear is retrieved by the theory. The migration of the disclination dipoles generates dislocation density dipoles, with partial Burgers vectors, whose glide parallel to the boundary and subsequent annihilation produces plastic shearing of the bicrystal. In addition to retrieving the core energy of the tilt boundaries at all misorientations, as shown in previous work (Taupin et al., 2013; Fressengeas et al., 2013), the theory allows capturing the correct two-folded dependence of the shear-migration coupling factor β on the misorientation angle. This result tends to confirm that disclinations are indeed appropriate objects for high-angle boundary modeling (Taupin et al., 2013). It is perhaps interesting to note that a finite strain formulation of the theory and nonlinearity of elasticity do not seem as essential for this purpose as nonlocal core elastic laws at interatomic scale. Although elastic dilatations as high as 20% are found in the defects core regions in the present calculations, using linear elasticity and a small strain formulation does not prevent from accurately retrieving the elastic energy of the grain boundaries and the shear-coupling factors. As viscous drag laws were employed for the mobility of defect densities, our results are restricted to moderate temperatures, a regime where grain boundary migration-type mechanisms are experimentally observed in Al, however (Gorkaya et al., 2009; Mompiou et al., 2009). At lower temperatures, where disclinations are likely to become less mobile, we expect that obstacle-overcoming kinetics could be more appropriate.

We believe that the present results demonstrate that an appropriate, continuous description involving displacement and crystal defect density fields that are smooth over a length scale of interatomic spacing can be adequate for the purpose of describing phenomena at this scale, and may usefully complement atomistic representations. A continuous description of the shear-coupled boundary migration, and more generally of the dynamics of crystal defect ensembles, may indeed be considered as attractive for several reasons. First, smoothness of the framework is desirable from the point of view of mathematical analysis and numerical computation, and because it allows coping with core properties. When viewed at a sufficiently small scale, lattice defects and the corresponding distributions of elastic strain and energy are certainly better described by suitably localized smooth density fields than by singularities. Interestingly and supporting this point of view, current work (Zimmerman et al., 2009; Tucker et al., 2010; Tucker et al., 2012) is devoted to designing metric tensors from the atomic displacements that result from molecular dynamics simulations, in order to post-process a continuous field description of the deformed atomistic configuration. In the shear-coupled boundary migration problem, the resulting plastic shear and rotation fields compare fairly well with our own findings. Further interest in considering a continuous framework may arise from its computational convenience because, as it does not have to resolve atomic vibrations with time steps in the femto-seconds, it is more tractable than atomistic simulations. By time coarse-graining, the atoms and their fast vibrations are indeed exchanged with the dissipative evolution of smooth dislocation/disclination density fields embedded in an elastic continuum. Finite element approximations then allow considering the dynamics of crystal defect ensembles over time scales in the *ms*, under realistic loading rates and stresses. The algorithms employed in the present work are detailed (Fressengeas et al., 2011). They are similar to those previously used in the pure dislocation dynamics case (Roy and Acharya, 2005; Varadhan et al., 2006). In the present two-dimensional simulations, they were coded in Fortran without using matrix optimization and parallel computing. Simulation times the order of 10*ms* were reached in less than half an hour of computing time on a single processor desktop computer. Realistic boundary migration rates, of the order of 0.1 μm/s were retrieved, in agreement with experimental data (Gorkaya et al., 2009). Diffusive phenomena and dislocation climb, which may have significant influence on grain boundary-mediated plasticity mechanisms (Winning et al., 2001; Mompiou et al., 2009; Priester, 2013), can therefore be investigated. Finally, beyond its capacity for representing individual crystal defects, the present continuous approach can seamlessly evolve into a coarse-grained mesoscale model for averaged crystal dislocation/disclination densities, able to reflect their self-organized behavior at larger polycrystal scale. This ability will be the object of future work. It will allow investigating alternative disclination-based mechanisms for plasticity, *e.g*, triple junction motion or emission/absorption of dislocations at grain boundaries, in media where dislocation-based plasticity is limited, either by scarcity of the slip systems in certain materials, or because dislocation glide is restricted, as in polynanocrystals.

Acknowledgement

The authors benefited of financial support from the ANR (Agence Nationale de la Recherche) under grant ANR-11-JS09-007-01, NanoMec.

References

Acharya, A., 2001. A model of crystal plasticity based on the theory of continuously distributed dislocations. J. Mech. Phys. Solids 49, 761.
Beausir, B., Fressengeas, C., 2013. Disclination densities from EBSD orientation mapping. Int. J. Solids Struct. 50, 137–146.
Berbenni, S., Paliwal, B., Cherkaoui, M., 2013. A micromechanical-based model for shear-coupled grain boundary migration in bicrystals. Int. J. Plast. 44, 68–94.
Bilby, B.A., 1955. Types of dislocation source. Bristol Conference Report on Defects in Crystalline Solids, 124. The Physical Society, London.
Cahn, J.W., Mishin, Y., Suzuki, A., 2006. Coupling grain boundary motion to shear deformation. Acta Mater. 54, 4953–4975.
deWit, R., 1970. Linear theory of static disclinations. In: Simmons, J.A., deWit, R., Bullough, R. (Eds.), Fundamental Aspects of Dislocation Theory, Spec. Publ. 317, vol. I. Nat. Bur. Stand., US, pp. 651–673.
Farkas, D., Froseth, A., Van Swygenhoven, H., 2006. Grain boundary migration during room temperature deformation of nanocrystalline Ni. Scr. Mater. 55, 695–698.
Frank, F.C. 1950. The resultant content of dislocations in an arbitrary intercrystalline boundary. In: Symposium on The Plastic Deformation of Crystalline Solids, Mellon Institute, Pittsburgh, (NAVEXOS-P-834), 150.
Fressengeas, C., Taupin, V., Capolungo, L., 2011. An elasto-plastic theory of dislocation and disclination fields. Int. J. Solids Struct. 48, 3499–3509.
Fressengeas, C., Taupin, V., Capolungo L. 2013. Continuous modeling of grain boundaries, (submitted for publication).
Gorkaya, T., Molodov, D.A., Gottstein, G., 2009. Stress-driven migration of symmetric ⟨001⟩ tilt grain boundaries in Al bicrystals. Acta Mater. 57, 5396.
Gurtin, M.E., Anand, L., 2008. Nanocrystalline grain boundaries that slip and separate: a gradient theory that accounts for grain-boundary stress and conditions at a triple junction. J. Mech. Phys. Solids 56, 184.
Gutkin, M.Yu., Ovidko, I.A., Skiba, N.V., 2003. Transformations of grain boundaries due to disclination motion and emission of dislocation pairs. Mater. Sci. Eng. A339, 73–80.
Khater, H.A., Serra, A., Pond, R.C., Hirth, J.P., 2012. The disconnection mechanism of coupled migration and shear at grain boundaries. Acta Mater. 60, 2007–2020.
Maranganti, R., Sharma, P., 2007. A novel atomistic approach to determine strain gradient elasticity constants: Tabulation and comparison for various metals, semiconductors, silica, polymers and the (Ir) relevance for nanotechnologies. J. Mech. Phys. Solids 55, 1823.
Mindlin, R.D., Tiersten, H.F., 1962. Effects of couple-stresses in linear elasticity. Arch. Ration. Mech. Anal. 11, 415.
Mompiou, F., Caillard, D., Legros, M., 2009. Grain boundary shear migration coupling I. In situ TEM straining experiments in Al polycrystals. Acta Mater. 57, 2198.
Nye, J.F., 1953. Some geometrical relations in dislocated crystals. Acta Metall. 1, 153.
Priester, L. 2013. Grain boundaries, from theory to engineering. Springer Series in Material Science, vol. 172. Springer Science+Business Media, Dordrecht.
Roy, A., Acharya, A., 2005. Finite element approximation of field dislocation mechanics. J. Mech. Phys. Solids 53, 143.
Taupin, V., Capolungo, L., Fressengeas, C., Das, A., Upadhyay, M., 2013. Grain boundary modeling using a theory of disclination and dislocation fields. J. Mech. Phys. Solids 61, 370.
Tucker, G.J., Zimmerman, J.A., McDowell, D.L., 2010. Shear deformation kinematics of bicrystalline grain boundaries in atomistic simulations. Model. Simul. Mater. Sci. Eng. 18, 1.
Tucker, G.J., Tiwari, S., Zimmerman, J.A., McDowell, D.L., 2012. Investigating the deformation of nanocrystalline copper with microscale kinematic metrics and molecular dynamics. J. Mech. Phys. Solids 60, 471–486.
Upadhyay, M., Capolungo, L., Taupin, V., Fressengeas, C., 2013. Elastic constitutive laws for incompatible crystalline media: the contributions of dislocations, disclinations and G-disclinations. Phil. Mag. 93 (7), 794–832.
Varadhan, S., Beaudoin, A.J., Acharya, A., Fressengeas, C., 2006. Dislocation transport using an explicit Galerkin/least-squares formulation. Model. Simul. Mater. Sci. Eng. 14, 2006.
Winning, M., Gottstein, G., Shvindlerman, L.S., 2001. Stress induced grain boundary motion. Acta Mater. 49, 211–219.
Zimmerman, J.A., Bammann, D.J., Gao, H., 2009. Deformation gradients for continuum mechanical analysis of atomistic simulations. Int. J. Solids Struct. 46, 238.